Real-time simulations of laser-induced electron excitations in crystalline ZnO

Xiao Chen [1,2,3,4] Thomas Lettau [3] Ulf Peschel [3] Nicolas Tancogne-Dejean [1,2,4,5] and Silvana Botti [1,2,3,4]

[1]*Research Center Future Energy Materials and Systems of the Research Alliance Ruhr, Germany*

[2]*Faculty of Physics and Astronomy and ICAMS, Ruhr University Bochum, Universitätstrasse 150, 44780 Bochum, Germany*

[3]*Institut für Festkörpertheorie und -optik, Friedrich-Schiller-Universität Jena, Max-Wien-Platz 1, 07743 Jena, Germany*

[4]*European Theoretical Spectroscopy Facility, 4000 Liege, Belgium*

[5]*Max Planck Institute for Structure and Dynamics of Matter and Center for Free-Electron Laser Science, Hamburg 22761, Germany*

(Received 21 March 2025; revised 20 October 2025; accepted 20 January 2026; published 25 February 2026)

We investigate nonequilibrium electron dynamics in crystalline ZnO induced by ultrashort, relatively intense, infrared laser pulses. Our focus is on understanding the mechanism that facilitates efficient conduction band population in ZnO to enable optically pumped lasing. We consider two different pulse frequencies (in the near infrared and mid infrared) for which experimental data are available, and we calculate the electronic response of a ZnO crystal for a wide range of pulse intensities. We apply and compare three complementary theoretical approaches: the analytical Keldysh model, the numerical solution of the semiconductor Bloch equations, and real-time time-dependent density functional theory. We conclude that time-dependent density functional theory is a valid *ab initio* approach for predicting conduction band population, that offers an accurate enough description of static and transient optical properties of solids and provides physics insight into the intermediate excitation regime, where electronic excitations are determined by the interplay of intraband tunneling, a consequence of band bending, and interband multiphoton absorption.

DOI: 10.1103/p3r8-6grq

I. INTRODUCTION

ZnO nanolasers are promising systems for applications in optoelectronics, offering electrically pumped laser capabilities that can be utilized in various fields such as optical communication, biosensing, medical imaging, and three-dimensional (3D) displays [1–4].

Since the initial report of lasing in ZnO in 1966 [5], over the subsequent decades, ZnO has been grown in various forms, including macroscopic single crystals [6], thin films [7], quantum wells [8], quantum rods (nanowires) [9], and quantum dots [10], all exhibiting substantial luminescence. Nanowires have attracted increased attention, as they fulfill all the requirements for realizing a nanolaser: ZnO serves as a well-studied gain medium, being a direct band-gap material with a large band-gap energy of 3.3 eV at 300 K [11], the end facets and cylindrical geometry of the nanowire precisely form a standalone Fabry-Pérot–type resonance cavity, and the available optical pump mechanism proves particularly useful, especially for biological applications [12]. In 2001, room-temperature laser emission from ZnO nanowires was reported for the first time [9].

While the potential of emerging ZnO nanolasers is promising, the key challenge lies in effectively injecting charge carriers to achieve sufficient gain and overcoming the significant optical losses inherent in such compact laser devices. A major drawback exists in the fundamental pumping mechanism: stimulated emission via linear optical processes in ZnO nanowires inherently requires intense, coherent deep-UV excitation sources. The excitation photon energy must surpass the band gap (∼3.3 eV) of ZnO nanowires for one-photon absorption pumping. Relying on expensive deep-UV pumping sources poses significant challenges to the widespread application of ZnO nanolasers due to overall cost, complexity, and incompatibility with chip-level integration.

An alternative approach under investigation for ZnO nanowires relies on an emission process induced by multi-photon absorption (MPA) [13–15]. When exposed to intense near-infrared (IR) radiation, the nonlinear interaction between the applied optical field and ZnO nanostructures results in the simultaneous absorption of two or more photons of sub-band-gap energy through a virtual-state assisted interband transition. This process generates electron-hole pairs, leading to band-edge emission via radiative recombination. Near-IR intense light pulses, readily produced with inexpensive laser diodes, thus offer a solution for chip-level design and low-cost implementation of ZnO nanolasers in photonic circuits and sensing systems.

Recently, Hollinger *et al.* reported a new experimental realization of a ZnO nanowire laser [16], demonstrating that varying the wavelength of the pumping pulse does not decrease the lasing threshold intensity I_{th}. In fact, by tuning the wavelength from the near infrared at 0.8 μm (1.55 eV) to the mid infrared at 3.5 μm (0.35 eV), the threshold intensity I_{th} changed only from 5×10^{15} to 6×10^{15} W/m^2. This observation suggests that the underlying electronic excitation

Published by the American Physical Society under the terms of the Creative Commons Attribution 4.0 International license. Further distribution of this work must maintain attribution to the author(s) and the published article's title, journal citation, and DOI.

mechanism undergoes modifications with variations of both pumping wavelength and intensity.

There are different regimes to describe electronic excitations in semiconductors. The first is the already mentioned single-photon absorption or linear-response regime, which requires a pumping photon energy $\hbar\omega_p$ larger than the band-gap energy E_g. It can be achieved with low intensities, long pump durations, and even continuous-wave pulses. Another regime is possible when $\hbar\omega_p < E_g$ and the pump intensity is sufficiently high, involving nonlinear electronic excitations. The dominant processes can be either multiphoton absorption (MPA) [13–15] or electron tunneling [17,18]. The latter is dominant for small values of $\hbar\omega_p$ and high pump intensity. In this case, the strong laser field bends the electronic bands, enabling direct tunneling of electrons from the valence bands to the conduction bands. Thus, the transition rate becomes independent of the photon energy, but solely depends on the intensity of the pumping light. In the lower intensity limit, MPA is a perturbative nonlinear process, where the strength of absorption of N photons scales as the Nth power of the laser intensity. Particularly interesting is the intermediate regime in which both the multiphoton-driven and field-driven mechanisms significantly contribute to the population of the conduction band.

Understanding the evolution of the electronic excitation mechanism due to varying pumping wavelengths and intensities holds profound implications for the optimization and practical utilization of ZnO nanowire lasers. Historically, many methods have been developed to describe light-matter interactions and predict carrier excitation densities for given laser pulses. Three methods have emerged as widely used approaches, employed by different communities, with increasing complexity and numerical cost: the Keldysh model, semiconductor Bloch equations, and *ab initio* methods such as time-dependent density functional theory.

The complementary nature of these approaches allows us to systematically assess which physical effects are crucial for accurate predictions and under what conditions simpler models remain reliable. This comparative framework provides valuable guidance for the broader community working on laser-matter interactions. Our study aims to systematically compare these different theoretical approaches and directly benchmark them against existing experimental results, enabling us to explain the observed variations in threshold intensities across different pulse wavelengths. This comparison enhances the fundamental understanding of carrier excitation in ZnO, and ultimately improves our understanding of ZnO nanowire laser operation.

The structure of this paper is as follows. Section II provides an introduction to the theoretical approaches: the Keldysh model (Sec. I A), the semiconductor Bloch equations (SBE) (Sec. I B), and time-dependent density functional theory (TDDFT) (Sec. I C). Section III A presents simulations of electron dynamics evolution under excitation pulses of varying intensities. Comparative analyses of simulations for near-infrared and mid-infrared pulses are detailed in Secs. III B and III C, respectively. Section III D discusses the effect of different propagation times, while Sec. III E focuses on the dynamical Franz-Keldysh effect for mid-infrared pumping. Further details on the calculation of dipole matrix elements, the impact of dephasing time on the SBE solution, the influence of band-gap errors on the SBE and Keldysh model, and the intensity-dependent optical parameters are elaborated in the Supplemental Material (SM) [19]. Throughout the paper, SI units are employed.

II. THEORY BACKGROUND AND METHODS

A. Keldysh model

The Keldysh model, introduced by Keldysh in 1964 [20], is a widely employed analytical theory to calculate light-induced excitation rates across a broad wavelength range. Keldysh originally developed this model to evaluate nonrelativistic ionization rates of hydrogenlike atoms and two-band solids subjected to strong laser fields, described in the length gauge and within the dipole approximation. To apply this approach to solids we rely on a two-band model in which the modifications of the band structure induced by the laser is translated into an effective band gap that takes into account the Stark shift of the energy levels and can therefore describe below-band-gap photon-assisted excitation [21].

According to the Keldysh model, MPA is the dominant process, for excitations at photon energies smaller than the band gap, when the dimensionless Keldysh parameter $\gamma = \omega\sqrt{m^* E_g}/eE$ [22] is large ($\gamma \gg 1$), while electron tunneling is the dominating mechanism for $\gamma \ll 1$. In the formula for γ, ω is the pump laser frequency, $m^* = 0.3\, m_e$ is the effective reduced mass of the electron and hole pair in units of the electron mass m_e, calculated from DFT + U band structure (details in Sec. II B), e is the absolute value of the electron charge, and E is the laser electric field strength. The strength of the electric field E is related to the pump laser intensity I,

$$I = \tfrac{1}{2} n \epsilon_0 c E^2, \tag{1}$$

where ϵ_0 is the vacuum dielectric permittivity, c is the vacuum speed of light, and the refractive index n is equal to 1 in air.

The excitation rate $W_{\mathrm{ex}}^{\mathrm{Keldysh}}$ in units of $\mathrm{m}^{-3}\,\mathrm{s}^{-1}$ denotes the number of excited electrons per unit volume and time, and it can be calculated using the following equations [20,22]:

$$W_{\mathrm{ex}}^{\mathrm{Keldysh}} = \frac{2\omega}{9\pi}\left(\frac{\sqrt{1+\gamma^2}}{\gamma}\frac{m^\star \omega}{\hbar}\right)^{3/2} Q\left(\gamma, \frac{\tilde{E}_g}{\hbar\omega}\right) \times \exp\left(\frac{-\pi k[K(\gamma_1) - E(\gamma_1)]}{E(\gamma_2)}\right), \tag{2}$$

with the dimensionless Coulomb factor

$$Q(\gamma, x) = \left(\frac{\pi}{2K(\gamma_2)}\right)^{1/2} \times \sum_{n=0}^{\infty}\left\{\exp\left(\frac{-\pi n[K(\gamma_1) - E(\gamma_1)]}{E(\gamma_2)}\right) \times \Phi\left[\left(\frac{\pi^2(2\lfloor x+1\rfloor - 2x + n)}{2K(\gamma_2)E(\gamma_2)}\right)^{1/2}\right]\right\}, \tag{3}$$

the renormalized band gap that considers the energy shift induced by the Stark effect

$$\tilde{E}_g = \frac{2}{\pi} E_g \frac{\sqrt{1+\gamma^2}}{\gamma} E(\gamma_2), \tag{4}$$

and the Dawson integral

$$\Phi(x) = \int_0^x \exp(y^2 - x^2)dy. \tag{5}$$

In the above equations, the parameters $\gamma_1 = \gamma/\sqrt{1+\gamma^2}$ and $\gamma_2 = 1/\sqrt{1+\gamma^2}$ are dimensionless, like γ. $K(x)$ and $E(x)$ are complete elliptic integrals of the first and second kind, respectively:

$$K(x) = \int_0^{\pi/2} (1 - x^2\sin^2\theta)^{-1/2}d\theta,$$
$$E(x) = \int_0^{\pi/2} (1 - x^2\sin^2\theta)^{1/2}d\theta. \tag{6}$$

We can define the order of the MPA using the parameter k:

$$k = \lfloor \frac{\tilde{E}_g}{\hbar\omega} + 1 \rfloor, \tag{7}$$

where $\lfloor \dots \rfloor$ denotes rounding down to the nearest integer. Once the excitation rate $W_{\text{ex}}^{\text{Keldysh}}$ is calculated, we can determine the population of the conduction band induced by a laser pulse with a specific intensity I_{p} and central frequency ω, when the medium is a crystalline material with a band gap E_{g}.

We note that the Keldysh model has some limitations: it is valid for not too strong laser fields and photon energies smaller than the band gap, it does not take actual band structures into account [21,23], and it overlooks electron-electron interactions and many-body effects, so we do not expect it to work well in all situations. However, the Keldysh model provides crucial physical insight into the fundamental excitation regimes (multiphoton vs tunneling) through the dimensionless Keldysh parameter γ. This analytical approach offers rapid assessment of excitation mechanisms across different field strengths and frequencies, serving as a valuable reference point for understanding the limiting cases captured by more sophisticated methods. Its computational efficiency also makes it practical for parameter space exploration.

B. Semiconductor Bloch equations

To address the limitations of the Keldysh model, we turn to the semiconductor Bloch equations (SBE), which offer significant advantages in capturing complex carrier dynamics, multiband effects, and many-body effects. SBE can take into account the calculated band structure of ZnO, allowing for a precise description of transitions and coupling effects, while the Keldysh model provides a simpler analytical description. Furthermore, dephasing effects can be included in the framework of the SBE [24].

One way [25] to derive the SBE is by starting with the Hamiltonian H_{SBE} that describes electrons in a crystalline potential with a light field $\boldsymbol{E}(t)$ coupled to the electronic system in the dipole approximation:

$$H_{\text{SBE}}(\boldsymbol{r}, t) = T + V(\boldsymbol{r}) + e\boldsymbol{r}\cdot\boldsymbol{E}(t). \tag{8}$$

The wave function $\Psi(\boldsymbol{r}, t)$ is the solution of the time-dependent Schrödinger equation (TDSE),

$$i\hbar\frac{\partial\Psi(\boldsymbol{r}, t)}{\partial t} = H_{\text{SBE}}(\boldsymbol{r}, t)\Psi(\boldsymbol{r}, t), \tag{9}$$

can be expanded into the basis of the time-independent Bloch states $\phi_n^{\boldsymbol{k}}(\boldsymbol{r})$ with time-dependent coefficient $a_n^{\boldsymbol{k}}(t)$ [25], where the indices indicate the band index and $\boldsymbol{k}$ point,

$$\Psi(\boldsymbol{r}, t) = \sum_{n,\boldsymbol{k}\in\text{BZ}} a_n^{\boldsymbol{k}}(t)\phi_n^{\boldsymbol{k}}(\boldsymbol{r}). \tag{10}$$

Then, we can rewrite the TDSE (9) using Eq. (10) and project onto the Bloch states, obtaining the equation of motion for the time-dependent density matrix $\hat{\rho}(t) = |\Psi(\boldsymbol{r}, t)\rangle\langle\Psi(\boldsymbol{r}, t)|$ with matrix elements $\rho_{mn}^{\boldsymbol{k}}(t) = a_m^{\boldsymbol{k}}(t)a_n^{\boldsymbol{k}*}(t)$ [25]:

$$i\hbar\frac{d\rho_{mn}^{\boldsymbol{k}}(t)}{dt} = \left(E_m^{\boldsymbol{k}} - E_n^{\boldsymbol{k}}\right)\rho_{mn}^{\boldsymbol{k}}(t) - i\hbar(1-\delta_{mn})\rho_{mn}^{\boldsymbol{k}}(t)/T_2$$
$$+ ie\boldsymbol{E}(t)\cdot\boldsymbol{\nabla}_{\boldsymbol{k}}\rho_{mn}^{\boldsymbol{k}}(t) + e\boldsymbol{E}(t)\cdot$$
$$\times\sum_l\left[\boldsymbol{d}_{ml}^{\boldsymbol{k}}\rho_{ln}^{\boldsymbol{k}}(t) - \boldsymbol{d}_{ln}^{\boldsymbol{k}}\rho_{ml}^{\boldsymbol{k}}(t)\right], \tag{11}$$

where $E_m^{\boldsymbol{k}}$ is the band energy and $\boldsymbol{d}_{mn}^{\boldsymbol{k}}$ is the dipole matrix element for transitions between the bands m and n with $n \neq m$, or the Berry connections for $m = n$. The band structure and dipole matrix elements can be obtained from knowledge of the Kohn-Sham energies and wave functions, calculated for ZnO within DFT + U, as detailed in Sec. II C.

We want to simulate the experimental pump-laser pulses used in Ref. [16]: a 30-fs pulse with a threshold intensity $I_{\text{th}}^{0.8} = 5\times10^{15}$ W/m^2 and a near-IR central wavelength of 0.8 μm and a 105-fs pulse with $I_{\text{th}}^{3.5} = 6\times10^{15}$ W/m^2 and a mid-IR central wavelength of 3.5 μm. We use the same pulse shape, but reduce the pulse duration to make TDDFT calculations feasible. The detailed discussions of different propagation times are in Sec. III D.

The shape of the simulated laser field outside the ZnO crystal is described by Eq. (12):

$$\boldsymbol{E}(t) = \begin{cases} E_0\sin(\omega t)\sin^2(\pi t/T)\boldsymbol{e}_z, & \text{if } 0 < t < T \\ 0, \quad \text{else.} \end{cases} \tag{12}$$

Here E_0 is the strength of the electric field, ω is the laser frequency, T is the pulse duration, the polarization direction $\boldsymbol{e}_z$ is aligned with the c axis of the hexagonal ZnO structure. For the near-IR 0.8-μm laser, we use a simulated pulse duration of $T = 12.1$ fs, and the total propagation time is 14 fs. For the mid-IR 3.5-μm laser, the pulse duration is $T = 31.5$ fs, and the total propagation time is 36.3 fs. The total propagation time must be longer than the pulse duration to read out a stable excitation electron number after the pulse ends. The same laser field is used for SBE and TDDFT calculations.

To describe the many-body effects, like electron-electron, electron-hole, and electron-phonon scattering, we introduce a phenomenological dephasing term at the right side of Eq. (11) with dephasing time T_2 [26], which describes all the incoherent loss processes involved. In literature, a commonly employed approach consist in defining T_2 as a fraction of an optical cycle ($T_2 \approx T_0/4$ [27]) or about 1 fs [28,29]. Such short T_2 raises important conceptual questions concerning the ultrafast decoherence processes for electronic excitations in solids [26].

The choice of T_2 significantly affects the excited electron density n_{ex}, which varies from 2×10^{25}/m^3 to 6×10^{24}/m^3

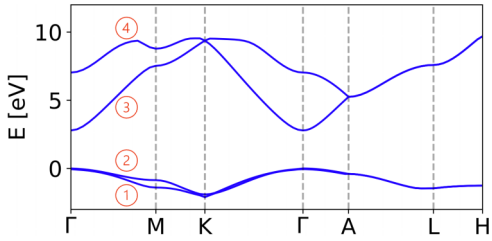


FIG. 1. Band structure of bulk ZnO computed for SBE using a four-bands model. We label the two valence bands as 1 and 2, and the two conduction bands as 3 and 4.

as T_2 increases from 10 fs to infinity. The effect of T_2 on the excitation densities is discussed in Sec. S2 of the SM [19]. Here we decide to set $T_2 = 20$ fs as we find it is a good compromise.

We note that there exist more complicated formulations of the SBE, including explicitly Coulomb interaction, excitonic effects [30], and Maxwell-SBE coupling [25]. In this work, these effects are not included. We employ the standard established form of SBE, which allows our results to be directly relevant to the broader literature.

We approximate the band structure of ZnO using a four-bands model (4BM). Figure 1 illustrates the band structure $E_m^{\boldsymbol{k}}$ of ZnO. In this figure, we show two valence bands (VBs), labeled as 1 and 2, and two conduction bands (CBs), labeled as 3 and 4, that constitute our 4BM. The calculations of $E_m^{\boldsymbol{k}}$ and $\boldsymbol{d}_{mn}^{\boldsymbol{k}}$ were conducted using the DFT + U method with a $12 \times 12 \times 41$ $\boldsymbol{k}$-points sampling grid across the entire Brillouin zone. The presence of degenerate bands along high-symmetry directions of the Brillouin zone for both VBs and CBs can lead to inaccuracies when using a simplified two-bands model (2BM), as the dipole matrix elements of degenerate levels can be very different (see Fig. S1 of the SM [19]). Employing a 4BM significantly mitigates these errors.

While full-band calculations would provide the most accurate description, our choice of a 4BM spanning approximately 15 eV is well justified for ZnO, a wide-band-gap insulator. Compared to narrow-gap semiconductors such as Si or GaAs, ZnO's large band gap and the photon energies involved in our simulations ensure that the selected band manifold is sufficient to capture the essential physics. The 4BM-SBE approach allows us to include band structure effects and coherent dynamics while maintaining computational tractability. This represents the standard approach used in the semiconductor optics community for understanding ultrafast carrier dynamics.

Given that the external laser is z polarized, we only need to consider the z components of the dipole matrix elements $\boldsymbol{d}_{mn}^{\boldsymbol{k}}$ (calculated matrix elements are shown in Sec. S1 of the SM [19]). The effective mass in the Keldysh model is calculated from the DFT + U band structure along the Γ-A direction, which coincides with the laser polarization axis. The obtained effective masses are $m_e^* = 0.338\, m_e$ for electrons and $m_h^* = -2.820\, m_e$ for holes, yielding a reduced effective mass of $m^* = 1/(1/m_e^* + 1/m_h^*) = 0.3\, m_e$.

When calculating the gradient term $\nabla_{\boldsymbol{k}} \rho_{mn}^{\boldsymbol{k}}(t)$ in Eq. (11), we enhance the resolution along the $\boldsymbol{k}_z$ direction by employing Akima one-dimensional (1D) interpolation [31] with periodic boundary conditions for both $E_m^{\boldsymbol{k}}$ and $\boldsymbol{d}_{mn}^{\boldsymbol{k}}$. This method utilizes a continuously differentiable subspline constructed from piecewise cubic polynomials. The interpolation increases the number of $\boldsymbol{k}_z$ points from 41 to 300, corresponding to a spacing of $\Delta \boldsymbol{k}_z = 0.04\ \mathrm{nm}^{-1}$.

For the initial condition of propagation, we set $\rho_{11}^{\boldsymbol{k}}(t=0) = \rho_{22}^{\boldsymbol{k}}(t=0) = 1$, with all other elements being zero. To solve the differential equations (11), we choose the 12th-order Adams-Bashforth method [32] due to its high accuracy and efficiency, and the time step Δt is set as 10^{-3} fs.

Then, we can calculate the density matrix elements for each time step. The number of electrons excited from VBs to CBs, $n_{\mathrm{ex}}^{\mathrm{SBE}}(t)$, is obtained as follows:

$$n_{\mathrm{ex}}^{\mathrm{SBE}}(t) = \frac{2}{V} \sum_{\boldsymbol{k}} w_{\boldsymbol{k}} \left[\rho_{33}^{\boldsymbol{k}}(t) + \rho_{44}^{\boldsymbol{k}}(t) \right], \tag{13}$$

where V is the unit-cell volume, $w_{\boldsymbol{k}}$ is the $\boldsymbol{k}$-point weight, the summation of $\boldsymbol{k}$ points is over the whole irreducible Brillouin zone, and the factor of 2 accounts for the spin of the electrons.

C. Time-dependent density functional theory

Time-dependent density functional theory (TDDFT) is an extension of DFT designed to calculate the properties of many-electron systems under the influence of time-dependent external potentials, such as electric or magnetic fields. Real-time TDDFT stands out as one of the most appealing methods for investigating electron dynamics under ultrashort laser pulse irradiation, enabling studies beyond linear response. The formal foundation of TDDFT is the Runge-Gross theorem [33] that establishes a unique mapping between the time-dependent external potential of a system and its time-dependent density $n(\boldsymbol{r}, t)$ for a given initial wave function. Our treatment employs TDDFT in the dipole (long-wavelength) approximation, where the electromagnetic fields are spatially uniform within the material. In this regime, the macroscopic current density required for Maxwell's equations is correctly obtained from the time-dependent density via $\boldsymbol{J}(t) = -d\boldsymbol{P}(t)/dt$, where $\boldsymbol{P}(t)$ is the macroscopic polarization obtained as $\boldsymbol{P}(t) = (1/V) \int \boldsymbol{r} n(\boldsymbol{r}, t) d^3 r$. This approach does not require current-density functional theory (CDFT), which becomes necessary only when treating spatially varying transverse fields at finite wave vectors. The $n(\boldsymbol{r}, t) = 2 \sum_{n,\boldsymbol{k} \in \mathrm{BZ}} |\psi_{n,\boldsymbol{k}}(\boldsymbol{r}, t)|^2$ is determined by solving an auxiliary set of Schrödinger equations, the time-dependent Kohn-Sham (TDKS) equations

$$i\hbar \frac{\partial \psi_{n,\boldsymbol{k}}(\boldsymbol{r}, t)}{\partial t} = H_{\mathrm{KS}}(\boldsymbol{r}, t) \psi_{n,\boldsymbol{k}}(\boldsymbol{r}, t). \tag{14}$$

Here, the indices n and $\boldsymbol{k}$ indicate the band index and $\boldsymbol{k}$ point, respectively. $\psi_{n,\boldsymbol{k}}(\boldsymbol{r}, t)$ is the time-dependent single-particle wave function. $H_{\mathrm{KS}}(\boldsymbol{r}, t)$ is the time-dependent Kohn-Sham Hamiltonian, and it can be written in velocity gauge [34], as shown in Eq. (15). The gauge transformation is employed to circumvent discontinuities arising from the

electric field propagation in periodic systems [35]:

$$H_{\mathrm{KS}}(\boldsymbol{r},t) = \frac{1}{2m_e}\left(\boldsymbol{p} + \frac{e}{c}\boldsymbol{A}_{\mathrm{tot}}(t)\right)^2 + V_{\mathrm{ion}}(\boldsymbol{r}) + V_{\mathrm{H}}(\boldsymbol{r},t) + V_{\mathrm{xc}}(\boldsymbol{r},t). \quad (15)$$

Here, the first term on the right side $\frac{1}{2m_e}(\boldsymbol{p} + \frac{e}{c}\boldsymbol{A}_{\mathrm{tot}}(t))^2$ includes the kinetic energy of electrons and the laser field, described in the velocity gauge, m_e, e, c, $\boldsymbol{p}$ denote the electron mass, elementary charge, vacuum light speed, and electron momentum, respectively. The potential terms V_{ion}, V_{H}, and V_{xc} indicate the pseudopotentials, the Hartree potential, and the exchange-correlation potential, respectively. We omitted here the nonlocal contribution to the external potential from the pseudopotentials for simplicity.

The total vector potential $\boldsymbol{A}_{\mathrm{tot}}(t)$ is time dependent and spatially uniform. It is composed of the external and induced vector potentials $\boldsymbol{A}_{\mathrm{tot}}(t) = \boldsymbol{A}_{\mathrm{ext}}(t) + \boldsymbol{A}_{\mathrm{ind}}(t)$. The external vector potential $\boldsymbol{A}_{\mathrm{ext}}(t)$ is related to the electric field of the applied laser pulse $\boldsymbol{E}_{\mathrm{ext}}(t)$ by

$$\boldsymbol{E}_{\mathrm{ext}}(t) = -\frac{1}{c}\frac{d\boldsymbol{A}_{\mathrm{ext}}(t)}{dt}, \quad (16)$$

where $\boldsymbol{E}_{\mathrm{ext}}(t)$ is described by Eq. (12). The same notation is applied to the total electric field $\boldsymbol{E}_{\mathrm{tot}} = \boldsymbol{E}_{\mathrm{ext}} + \boldsymbol{E}_{\mathrm{ind}}$. The induced macroscopic vector potential is given by the Maxwell equation

$$\frac{\partial^2}{\partial t^2}\boldsymbol{A}_{\mathrm{ind}}(t) = \frac{4\pi c}{V}\boldsymbol{J}(t), \quad (17)$$

with cell volume V and macroscopic current $\boldsymbol{J}(t)$ [36,37], and $\boldsymbol{J}(t)$ can be calculated from Eq. (18),

$$\boldsymbol{J}(t) = \frac{-i}{V}\int d\boldsymbol{r}\sum_{n,\boldsymbol{k}}\psi^*_{n,\boldsymbol{k}}(\boldsymbol{r},t)[\hat{H}_{\mathrm{KS}}(\boldsymbol{r},t),\hat{\boldsymbol{r}}]\psi_{n,\boldsymbol{k}}(\boldsymbol{r},t), \quad (18)$$

this self-consistent treatment of the induced field arising from macroscopic current is a key advantage of TDDFT, particularly for describing ultrafast and nonlinear phenomena.

We perform TDDFT calculations with periodic boundary conditions of the bulk ZnO crystal. This means that we directly apply a rescaled "internal" field to the infinite bulk crystal and compute the dielectric response without explicit consideration of surface and vacuum interfaces. We need therefore to establish the correct field amplitude inside the material based on the external field given by experiment and the boundary conditions at the surface. Linear Fresnel relations are still (approximately) appropriate for this purpose, as the linear coefficient dominates the overall response at our field intensities, following the approach explained and validated in Refs. [23,38]. The nonlinear electronic dynamics inside the crystal are fully captured by TDDFT with the rescaled field as input.

There are two different ways to proceed that give approximately the same rescaled field. We consider and compare both, calling them "modified" and "unmodified" calculations. A detailed description of these approximations can be found in Sec. III A.

The second term of Eq. (15), $V_{\mathrm{ion}}(\boldsymbol{r})$, describes the electron-ion interaction. We employ Pseudodojo PBE norm-conserving pseudopotentials [39] to describe the interaction between ions and valence electrons. These pseudopotentials account for the 6 valence electrons of the oxygen atom ($2s^2 2p^4$) and 20 valence electrons of the zinc atom ($3s^2 3p^6 3d^{10} 4s^2$). The energy transfer from electrons to ions is ignored by freezing the ionic position, so it is time independent.

The third term $V_{\mathrm{H}}(\boldsymbol{r},t) = e^2\int d\boldsymbol{r}'\frac{n(\boldsymbol{r},t)}{|\boldsymbol{r}-\boldsymbol{r}'|}$ is the Hartree potential, which describes the classical part of the electron-electron interaction.

The fourth term $V_{\mathrm{xc}}(\boldsymbol{r},t)$ is the exchange-correlation potential. In this work, we utilize the adiabatic generalized gradient approximation functional proposed by Perdew, Burke, and Ernzerhof (GGA-PBE) in 1997 [40]. It is acknowledged that the GGA Kohn-Sham band gap significantly underestimates the experimental quasiparticle gap. In this case, the calculated GGA-PBE direct band gap is 0.79 eV, while the experimental direct band-gap value is 3.3 eV [11]. The appropriate band-gap value is crucial for the excitation properties' calculations. To open the gap, we employ the DFT + U method, which is extended to the TDDFT scheme in Ref. [41], resulting in an improved Kohn-Sham band-gap energy of 2.81 eV. The fundamental idea behind DFT + U is to address the strong onsite Coulomb interaction of localized electrons by introducing an additional Hubbard-type term. We include the Hubbard energy E_U in the DFT total energy, and E_U is dependent solely on the effective Hubbard U parameter U_{eff}. This parameter can be extracted from *ab initio* calculations or set empirically. In this work, we adopt the values of $U_{\mathrm{eff}} = 12.8$ eV for $3d$ orbitals of zinc atoms and $U_{\mathrm{eff}} = 5.29$ eV for $2p$ orbitals of oxygen atoms, which were determined *ab initio* using the ACBN0 functional in Ref. [42]. This approach provides a variational treatment superior to empirical scissor operators, as it modifies the ground-state electronic structure rather than applying *post hoc* energy corrections. Although the U_{eff} applied to the p electrons is not as well justified from a theoretical perspective as for d electrons, it is a common and effective choice for obtaining improved band gaps in wide-band-gap insulators.

The number of electrons excited from the valence to the conduction bands, $n_{\mathrm{ex}}^{\mathrm{TDDFT}}(t)$, can be calculated in the TDDFT framework [34] as

$$n_{\mathrm{ex}}^{\mathrm{TDDFT}}(t) = \frac{2}{V}\sum_{nn'\boldsymbol{k}} w_{\boldsymbol{k}}(\delta_{nn'} - |\langle\phi_{n\boldsymbol{k}}|\psi_{n'\boldsymbol{k}}(t)\rangle|^2). \quad (19)$$

Here n, n' are the band indices, $\boldsymbol{k}$ is the Bloch wave number, $w_{\boldsymbol{k}}$ is the $\boldsymbol{k}$-point weight, $\phi_{n\boldsymbol{k}}$ is the ground-state Kohn-Sham wave function, $\psi_{n'\boldsymbol{k}}(t)$ is the time-evolved wave function, $V = 49.668$ Å^3 is the volume of unit cell, and the factor of 2 accounts for the spin of the electrons.

The quantity $n_{\mathrm{ex}}^{\mathrm{TDDFT}}(t)$ is not a physical observable, but rather an analysis tool derived from projecting the time-evolved Kohn-Sham states onto the ground-state Kohn-Sham basis. This requires approximating the many-body density matrix by the Kohn-Sham single-particle density matrix, which is a significant approximation, as individual matrix elements of the Kohn-Sham density matrix can differ substantially from those of the true many-body system. However, when we calculate the electron density, we sum over all occupied states rather than treating individual matrix elements

separately. If we consider the complete set of Kohn-Sham orbitals (occupied and unoccupied), the sum of all matrix elements, i.e., the trace of the density matrix, always equals the total number of electrons in the system. Summing over the originally occupied KS orbitals therefore corresponds to taking the partial trace in the subspace formed by the initial equilibrium states, and thus provides a measure of how many electrons have been excited. Although coherence and decoherence effects encoded in the off-diagonal terms are not captured in our analysis, the diagonal components still yield a meaningful estimate of electron excitation. Kohn-Sham band populations have been shown to correlate well with experimental observables in ultrafast spectroscopy, such as transient absorption spectra and photoemission signals [43]. This projection thus provides an intuitive and practical measure of excitation dynamics within the TDDFT framework. A similar approximation, replacing true many-body wave function with TD(KS) Slater determinants, is also used in the same TDDFT framework to compute ionization probabilities and photoelectron spectra [44].

The DFT and TDDFT calculations were performed in the Kohn-Sham scheme using octopus [45,46], a real-time, real-space package that makes use of pseudopotentials to simulate the electron-ion dynamics of one-, two-, and three-dimensional finite and periodic systems subject to time-dependent electromagnetic fields.

Crystalline ZnO possesses a hexagonal wurtzite crystal structure, falling within the $P6_3mc$ space group (No. 186). The primitive cell comprises 2 zinc atoms and 2 oxygen atoms. The optimized lattice parameters, calculated within DFT with the GGA-PBE functional [40], are $a = b = 3.289$ Å, $c = 5.307$ Å, $\alpha = \beta = 90^\circ$, and $\gamma = 120^\circ$, exhibiting a 1.21% deviation from the room-temperature x-ray-diffraction experimental data [47]: $a = b = 3.250$ Å, $c = 5.204$ Å. This results in a DFT primitive cell volume of 49.668 Å^3. Periodic boundary conditions were applied to the primitive cell.

The wave functions, densities, and potentials were discretized with a real-space mesh grid with spacing 0.1 Å which is equivalent to the grid cutoff energy $E_{\text{cut}} = 3.3$ keV. The $\boldsymbol{k}$-point sampling method in reciprocal space followed the Monkhorst-Pack scheme [48], the grid was set as $12 \times 12 \times 7$, which corresponds to 1008 $\boldsymbol{k}$ points in the whole Brillouin zone, with convergence precision of 4 meV/atom.

The external laser field in Eq. (12) was produced to impinge on the simulation box with the polarization along the z direction, breaking the symmetry in this direction. So we can utilize the remaining 6 symmetries of the system, and reduce the $\boldsymbol{k}$-points sampling number from 1008 to 217. The time step is chosen as $\Delta t = 3.6 \times 10^{-4}$ fs after thorough convergence tests.

The propagator algorithm employed the enforced time-reversal symmetry method [49], where the wave function at time step $(n+1)$ can be calculated by the information of time step n: $\psi_{n+1} = \exp(-i\delta t H_{n+1}/2)\exp(-i\delta t H_n/2)\psi_n$. The Hamiltonian H_{n+1} is estimated by a single exponent $\psi^*_{n+1} = \exp(-i\delta t H_n)\psi_n$ and $H_{n+1} = H[\psi^*_{n+1}]$. We choose the default fourth-order Taylor expansion for the time-evolution operator $\exp(-i\delta t H) = \sum_{i=0}^{4} \frac{(-i\delta t)^i}{i!} H^i$, as recommended in Ref. [50]. Since the Kohn-Sham propagator is nonlinear, for each propagation step we perform the self-consistent correction to decrease the propagation error, using a self-consistency accuracy threshold of 0.03 meV.

We note that the SBE can be connected with TDDFT. Turkowski and coworkers [51] developed a TDDFT version of SBE, which formulate TDDFT in terms of the density matrix. By replacing the Kohn-Sham Hamiltonian H_{KS} in Eq. (15) with the SBE Hamiltonian H_{SBE} in Eq. (8), then the TDSE (9) yields the TDDFT version of the SBE. More details can be found in Refs. [51,52].

We remark that the experimental band gap of ZnO is $E_{\text{g}} = 3.30$ eV [11], while our DFT + U value is 2.81 eV. To maintain consistency in the comparison of the different theoretical approaches, we decided to use the value of 2.81 eV for the calculations using SBE and the Keldysh model. Similarly, the volume employed is always the one obtained from DFT relaxation. The effects of the band-gap discrepancy are further discussed in Sec. S3 of the SM [19].

III. RESULTS AND DISCUSSION

In our analysis, we examine various pump laser wavelength scenarios and compare the number of excitation electrons calculated with all three models $n_{\text{ex}}^{\text{Keldysh}}$, $n_{\text{ex}}^{\text{SBE}}$, and $n_{\text{ex}}^{\text{TDDFT}}$.

For the TDDFT and SBE calculation, we define the calculated excitation electron numbers $n_{\text{ex}}^{\text{SBE}}$ and $n_{\text{ex}}^{\text{TDDFT}}$, as the stable readout value after the end of the pumping pulse, when no external vector potential is present anymore. In contrast, the Keldysh model yields a cycle-averaged excitation rate $W_{\text{ex}}^{\text{Keldysh}}$. To compare with the other models, we estimate the total excited carrier density from the Keldysh model as

$$n_{\text{ex}}^{\text{Keldysh}} = W_{\text{ex}}^{\text{Keldysh}} T, \tag{20}$$

where T is the pulse duration. This approach assumes a quasiconstant field strength during the pulse and should yield a larger n_{ex} compare to TDDFT and SBE, which use the $\sin^2$ pulse.

To achieve the laser emission, one of the necessary conditions is population inversion, which requires the electron density in the conduction band arrive at the threshold; here we use the reference value $n_{\text{th}}^{\text{Ref}} = 2 \times 10^{25}/\text{m}^3$, suggested for bulk ZnO in Refs. [16,53]. The comparison is discussed in Sec. III D.

A. Electron dynamics evolution

In Fig. 2, we show the evolution of the density of excited electrons n_{ex}, in response to the external pump laser. The upper panel illustrates the near-IR external electric field $\boldsymbol{E}_{\text{ext}}$, with a wavelength $\lambda = 0.8$ μm, a photon energy $\hbar\omega = 1.55$ eV, and a field strength $E_0 = 0.13$ V/Å, which corresponds to an intensity of 2.2×10^{15} W/m^2. The middle panel shows the evolution of the excited electron density n_{ex} obtained from the SBE, with the 4BM depicted in blue and the 2BM in red. The bottom panel presents the evolution of n_{ex} calculated using TDDFT, an inset provides a zoomed-in view near the end of the pulse. The readout values of n_{ex} at the end of pulse duration $T = 12.1$ fs for each method are listed in Table I.

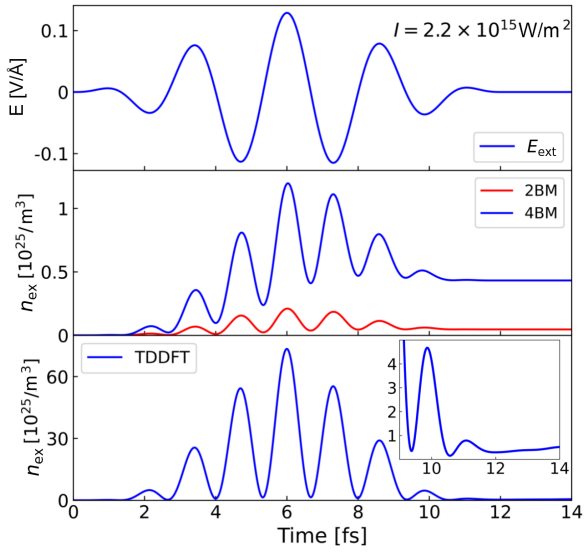


FIG. 2. Electron dynamics evolution of ZnO. The top panel shows the external pump laser field $\boldsymbol{E}_{\text{ext}}$. The middle panel displays the evolution of the excited electron density $n_{\text{ex}}(t)$ according to the SBE, with a 4BM (blue) and a 2BM (red). The bottom panel illustrates the evolution of $n_{\text{ex}}(t)$ in TDDFT. The pump laser intensity is 2.2×10^{15} W/m^2.

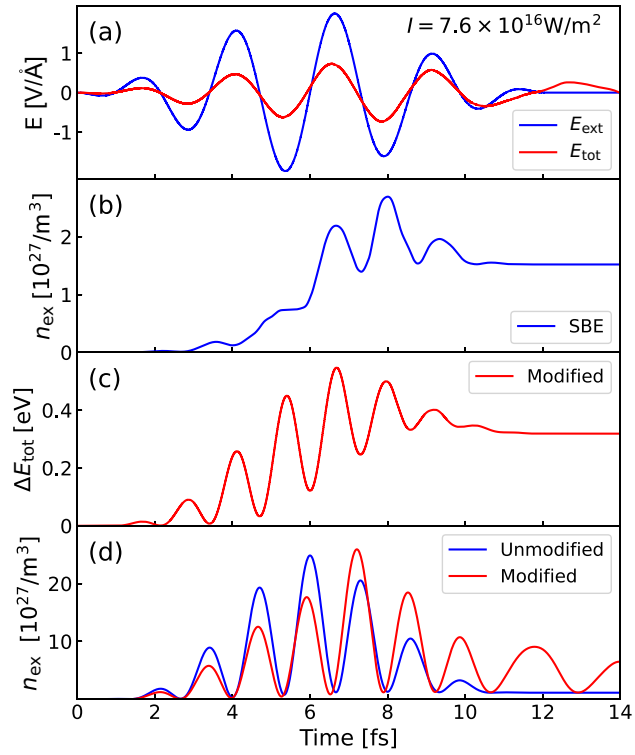


FIG. 3. Electron dynamics evolution of ZnO. (a) Shows the external electric field $\boldsymbol{E}_{\text{ext}}$ (blue), and the total electric field $\boldsymbol{E}_{\text{tot}}$ (red) of TDDFT. (b) Displays the evolution of the excited electron density $n_{\text{ex}}(t)$ for SBE with 4BM. (c) Illustrates the change in total energy ΔE_{tot} for the "modified" case of TDDFT. (d) Displays the evolution of $n_{\text{ex}}(t)$ for the "modified" case (red) and the "unmodified" case (blue) of TDDFT, details in script. The pump intensity is 7.6×10^{16} W/m^2.

Notably, the n_{ex} obtained from the 2BM approach is an order of magnitude lower than that from the other two methods. One reason for this discrepancy is due to broken bands degeneracies (see Fig. 1) and the consequent loss of oscillator strength for the transitions along high-symmetry lines. Another important factor is the inherent limitation of a 2BM, which is often insufficient to fully describe electron dynamics. Similar conclusions have been drawn for high-harmonic generation in solids at comparable laser intensities, where up to 51 bands needed to be included for accurate results using the SBE [54]. For higher intensities, numerical instabilities become significant in the SBE calculation. In Fig. 3, the external laser intensity is 7.6×10^{16} W/m^2. Figure 3(b) displays the evolution of the excited electron density $n_{\text{ex}}(t)$ for SBE with the 4BM. Under this intensity, electrons tend to transition to higher-energy bands, and even the 4BM is insufficient to fully describe the electron behavior, leading to some discordant parts in the evolution curves. Therefore, in the following, we restrict ourselves to pump intensity for SBE below 2×10^{16} W/m^2.

Before discussing the TDDFT data, the definition of the laser intensity needs to be clarified. The pulse intensity mentioned throughout the paper is the intensity measured outside the crystal, as per experimental convention. However, the corresponding intensity in the crystal during the TDDFT simulation requires careful treatment since the electric displacement and the electric field inside the material do not match due to the induced electric field created by the current in the material.

TABLE I. Density of excited carriers at the end of the laser pulse from the different models.

Method	n_{ex} (1/m^3)
2BM	4.61×10^{23}
4BM	4.32×10^{24}
TDDFT	2.94×10^{24}

The value of the intensity has to be consistent with the vector potential included in Eq. (15). If we substitute $\boldsymbol{A}_{\text{ext}}(t)$ for $\boldsymbol{A}_{\text{tot}}(t)$, the laser intensity used in simulation is the same as the experimental value outside the crystal, corresponding to the vector potential $\boldsymbol{A}_{\text{ext}}(t)$. We denote this scenario as the "unmodified" case, as we are not modifying the laser intensity compared to its value in vacuum. This approach, for example, was utilized for comparative analysis with the Keldysh model for crystalline silicon in Ref. [23].

When employing $\boldsymbol{A}_{\text{tot}}(t)$ in Eq. (15) for the dynamic calculation, we must consider that the total field experienced by electrons inside ZnO differs from the external field $\boldsymbol{A}_{\text{ext}}(t)$ due to the induced field created by the source term (current) in the material. The longitudinal part of the induced field is captured by the Hartree term of TDDFT, but the transversal contribution must be added by coupling to Maxwell equation, as explained above.

Rather than using linear-response optical constants, we account for this through an intensity-dependent effective dielectric function $\epsilon_{\text{eff}}(I)$ computed directly from our TDDFT

simulations [36,38]:

$$\frac{1}{\epsilon_{\text{eff}}(\omega, I)} = 1 + \frac{\int_{0_+}^{T} e^{i\omega t} \cdot \frac{d\boldsymbol{A}_{\text{ind}}(t)}{dt}\, dt}{\int_{0_+}^{T} e^{i\omega t} \cdot \frac{d\boldsymbol{A}_{\text{ext}}(t)}{dt}\, dt}. \tag{21}$$

This expression captures the complete time-dependent response of the system, including both linear and nonlinear effects, by directly relating the induced and external vector potentials. It reflects the full nonlinear dynamics of the medium under strong-field excitation, with ϵ_{eff} varying significantly with intensity as shown in our results.

The relationship $\boldsymbol{E}_{\text{ext}}/\text{Re}\{\epsilon_{\text{eff}}\} \approx \boldsymbol{E}_{\text{tot}}$ provides excellent agreement with our self-consistent calculations. For example, in Fig. 3(a), the external laser field $\boldsymbol{E}_{\text{ext}}$ has a strength of 2.007 V/Å, while the self-consistently calculated total field $\boldsymbol{E}_{\text{tot}}$ has a strength of 0.734 V/Å. Using our computed $\text{Re}\{\epsilon_{\text{eff}}\} = 2.710$, we obtain $\boldsymbol{E}_{\text{ext}}/\text{Re}\{\epsilon_{\text{eff}}\} = 0.741$ V/Å, differing from $\boldsymbol{E}_{\text{tot}}$ by only 0.9%.

To calculate the inner-crystal intensity I_{in}, we use the self-consistently determined total field $I_{\text{in}} = n\epsilon_0 c\boldsymbol{E}_{\text{tot}}^2/2$, yielding $I_{\text{in}} = 7.15 \times 10^{16}$ W/m^2 for the example above.

The outer-crystal intensity I_{out} can be calculated from I_{in} using $I_{\text{out}} = I_{\text{in}}/(1-R)$, where the reflectivity R for normal incidence, derived from the electromagnetic boundary conditions at the vacuum-solid interface [55], is

$$R = \left|\frac{n + i\kappa - 1}{n + i\kappa + 1}\right|^2, \tag{22}$$

with the complex refractive index components obtained from the intensity-dependent effective dielectric function

$$n = \sqrt{\frac{(|\epsilon_{\text{eff}}| + \text{Re}\{\epsilon_{\text{eff}}\})}{2}},\ \kappa = \sqrt{\frac{(|\epsilon_{\text{eff}}| - \text{Re}\{\epsilon_{\text{eff}}\})}{2}}. \tag{23}$$

All optical parameters $\epsilon_{\text{eff}}(\omega)$, complex refractive index $N(\omega) = n(\omega) + i\kappa(\omega)$, and reflectivity $R(\omega)$ are intensity dependent. Detailed values for different intensity points are provided in Sec. S4 of the SM [19].

In the case of ZnO in Fig. 3, the calculated $n = 1.647$, $\kappa = 0.039$, and the reflectivity R is 6%. Therefore, the outer-crystal intensity I_{out} is 7.6×10^{16} W/m^2 as indicated in Fig. 3(a). Due to the above-described modification process, we refer to this case as "modified." The TDDFT results of the bottom panel in Fig. 2 are also obtained with this "modified" procedure and the outer-crystal intensity is 2.2×10^{15} W/m^2.

Figure 3(c) shows the evolution of the total energy difference $\Delta E_{\text{tot}}(t)$ in eV for the "modified" case. The evolution of the excited electron number $n_{\text{ex}}(t)$ for the "modified" case (red) is shown in Fig. 3(d). The applied $\boldsymbol{E}_{\text{ext}}$ field ends at 12.1 fs, but the corresponding $\boldsymbol{E}_{\text{tot}}$ and n_{ex} still exhibit oscillations until the end of the pulse at 14 fs. Reference [34] attributes this behavior to plasma oscillations of the excited electrons in the conduction bands. Indeed, as no dissipation mechanism is included, the total energy is conserved, but transfer of energy will occur between the electrons and the Maxwell field, leading to oscillations in the induced vector potential.

To correct this, one can employ a gauge-dependent definition of the ground-state orbitals as Ref. [34]. We assume that the gauge field $\boldsymbol{A}(t)$ is slowly varying and spatially uniform. Then, the ground-state orbitals can be adiabatically evolved by replacing the Bloch wave number $\boldsymbol{k}$ with $\boldsymbol{k} + \boldsymbol{A}(t)$ and replacing the Bloch wave functions $\phi_{n\boldsymbol{k}}$ with $\phi_{n\boldsymbol{k}+\boldsymbol{A}(t)}$. Since the entire $\boldsymbol{k}$ region is occupied in the dielectrics, this adiabatic evolution does not produce any real excitation. Consequently, compared to $n_{\text{ex}}^{\text{TDDFT}}(t)$ in Eq. (19), the corrected normalized density of excited electrons $n_{\text{ad}}^{\text{TDDFT}}(t)$ can be calculated with respect to the adiabatically evolved orbitals

$$n_{\text{ad}}^{\text{TDDFT}}(t) = \frac{2}{V}\sum_{nn'\boldsymbol{k}} w_{\boldsymbol{k}}(\delta_{nn'} - |\langle\phi_{n\boldsymbol{k}+\boldsymbol{A}(t)}|\psi_{n'\boldsymbol{k}}(t)\rangle|^2). \tag{24}$$

The "modified" result can therefore be obtained by connecting the minima of the oscillations [34] of the red curve in the bottom panel of Fig. 3. This enables us to read out the stable value of $n_{\text{ex}} = 1.146 \times 10^{27}/\text{m}^3$ using the minimum points after the pulse ends for the "modified" case.

We can now compare with the results obtained in the "unmodified" case. This approach has the additional advantage that it does not include the computational cost of the induced vector potential and is therefore faster by a factor of 2 than calculations in the "modified" case. The evolution of $n_{\text{ex}}(t)$ for the "unmodified" case is depicted by the blue curve in Fig. 3(d). We can observe a perfectly flat line after the pulse ends at 12.1 fs, with a final value of $n_{\text{ex}} = 1.126 \times 10^{27}/\text{m}^3$.

This value is very close to the one obtained in the "modified" calculation (1.7% difference) at a reduced computational cost. The n_{ex} of the "unmodified" case is slightly lower than the one calculated in the "modified" case.

Based on our systematic comparison, we recommend the following best practices for TDDFT field treatment: The "modified" scheme, which includes the self-consistently induced vector potential, should be considered the theoretical gold standard as it accounts for the total electric field experienced by electrons. This approach is formally more accurate, especially for capturing nonlinear and field-induced effects, and we adopt it for the 0.8-μm case where quantitative comparison with experiment is crucial.

However, the "unmodified" scheme, based solely on the externally applied vector potential, provides a remarkably good approximation, yielding results within a few percent of the "modified" scheme while offering substantial computational savings. For extended simulations such as the mid-IR excitation case (3.5 μm), this efficiency advantage becomes essential for feasibility. The choice between schemes should be made deliberately based on the balance between required accuracy and computational constraints.

B. Near-infrared pump laser

In Fig. 4, we compare the calculated excited electron number per unit volume n_{ex} in m^{-3} for different pump intensities considering all three calculation methods: Keldysh (red), SBE (orange), TDDFT (blue, "modified"). The pump is a near-IR laser with a wavelength $\lambda = 0.8$ μm and a photon energy $\hbar\omega = 1.55$ eV. The laser intensity ranges from 2×10^{15} to 6×10^{17} W/m^2. The Keldysh parameter γ is recorded on the upper x axis.

In the Keldysh calculation points (red circles), a distinct discontinuity is highlighted by a green rectangular frame. This region encompasses two data points corresponding to pump intensities $I = 1.34 \times 10^{16}$ and 1.62×10^{16} W/m^2,

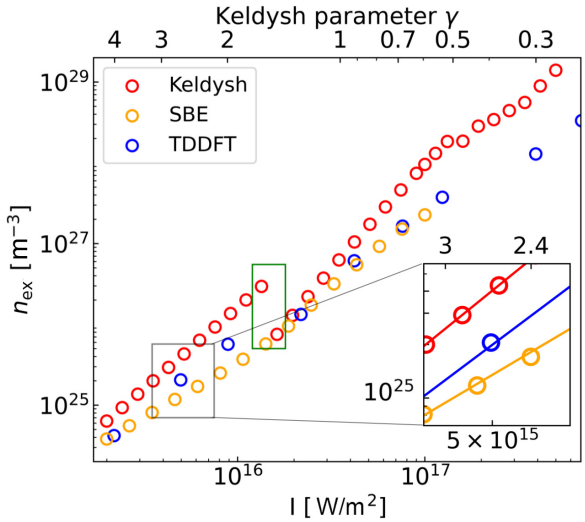


FIG. 4. The density of excited electrons n_{ex} for different pump laser intensity I. The data points are Keldysh (red), SBE (orange), and TDDFT (blue). The Keldysh parameter γ is recorded on the upper x axis. The near-IR pump laser has a wavelength $\lambda = 0.8$ μm corresponding to a photon energy of $\hbar\omega = 1.55$ eV.

with values of $(\frac{\tilde{E}_g}{\hbar\omega} + 1)$ being 2.98 and 3.01, respectively. As $k = \lfloor \frac{\tilde{E}_g}{\hbar\omega} + 1 \rfloor$ in Eq. (7) indicates the k-photon absorption process, these data points correspond to the transition from two-photon absorption (2PA) to three-photon absorption (3PA) regimes in the Keldysh model, respectively, leading to the observed discontinuity.

In the double-logarithm coordinate system, the linear relation signifies that the excited electron density n_{ex} is proportional to the mth power of pump intensity I_p: $\log(n_{ex}) \propto \log(I_p^m) \propto m \log(I_p)$, where m denotes the slope. The value of m does not necessarily coincide with the k of Keldysh model.

For the initial 11 Keldysh points from 2.00×10^{15} to 1.34×10^{16} W/m^2, $k = 2$ and $m = 2.01$, indicating the predominance of a 2PA mechanism. However, for the next 13 Keldysh points from 1.62×10^{16} to 1.32×10^{17} W/m^2, $k = 3$ and $m = 2.33$, the corresponding Keldysh parameter γ varies from 1.47 to 0.52. This indicates that the absorption mechanism is not only due to 3PA but also involves tunneling ionization.

The inset of Fig. 4 provides a magnified view of the calculation points in a specific region of interest, near the experimental threshold intensity $I_{th}^{0.8} = 5 \times 10^{15}$ W/m^2 [16]. For each calculation method, we performed a linear fitting of the low-intensity points, specifically, 11 for Keldysh (2.00×10^{15} to 1.34×10^{16} W/m^2), 3 for TDDFT (2.19×10^{15} to 8.89×10^{15} W/m^2), and 10 for SBE (2.00×10^{15} to 3.27×10^{16} W/m^2). This procedure allows us to accurately extract by interpolation the n_{ex} value at $I_{th}^{0.8}$. The slope m of the linear fitting curve and the corresponding density of excited electrons n_{ex} at $I_{th}^{0.8}$ are reported in Table II.

We note that we employ a sin^2 envelope. It was shown in Ref. [56] that this leads to reliable power-law fitting compared to other envelopes, for the range of intensities considered here. For the near-IR pulse (λ=0.8 μm), in the vicinity of $I_{th}^{0.8}$, the Keldysh model exhibits a slope m exactly equal to 2.01,

TABLE II. Comparison of the slope m and excited-electron density n_{ex} according to the different calculation methods for $\lambda = 0.8$ μm.

Method	m	n_{ex} (m^{-3})
Keldysh	2.01	4.0×10^{25}
SBE	1.47	1.4×10^{25}
TDDFT	1.86	1.99×10^{25}

clearly indicating a 2PA mechanism. In contrast, TDDFT and SBE have slopes m of 1.86 and 1.47, respectively, hence smaller than 2. This suggests that the excitation mechanism is 2PA dominated but also involves some degree of tunneling assistance. Such differences between the models are expected as the Keldysh model simplifies the band structure to two energy levels and is no more valid at very high field intensities.

For the comparison of n_{ex}, the Keldysh model uses the same pulse propagation time of 12.1 fs as employed in TDDFT and SBE. However, it assumes a constant electric field at the peak amplitude throughout the duration, whereas TDDFT and SBE adopt a sin^2 pulse shape. As a result, the Keldysh model yields a significantly larger n_{ex} value. Due to its inclusion of more bands than the four-band SBE model, TDDFT enables excitations to higher-energy levels, resulting in a larger slope m and higher n_{ex}. The effect of propagation time is discussed in Sec. III D, and the role of the SBE dephasing time T_2 is addressed in S2 of the SM [19].

C. Mid-infrared pump laser

Now, we turn to the mid-IR case. The pump laser has a wavelength $\lambda = 3.5$ μm and a corresponding photon energy $\hbar\omega = 0.354$ eV. In Fig. 5, we compare the excited electron density n_{ex}(per m^3) across different pump intensities for all calculation methods: Keldysh (red), SBE (orange), and

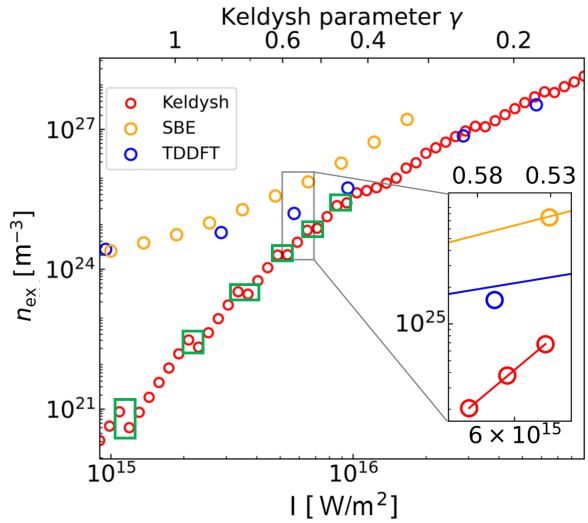


FIG. 5. Same as Fig. 4, but for a mid-IR pump laser with a wavelength $\lambda = 3.5$ μm corresponding to a photon energy of $\hbar\omega = 0.354$ eV.

TABLE III. Comparison of the slope m and excited-electron density n_{ex} according to the different calculation methods for $\lambda = 3.5$ μm.

Method	m	n_{ex} (m^{-3})
Keldysh	6.42	4.18×10^{24}
SBE	1.97	6.4×10^{25}
TDDFT	1.26	2.2×10^{25}

TDDFT (blue; "unmodified"). The Keldysh parameter γ is shown on the upper x axis.

In the Keldysh data, discontinuous regions are highlighted by green rectangular frames. They indicate changes in the parameter k of Eq. (7). The lowest frame illustrates the conversion of k from 9PA to 10PA as the intensity increases from 9.89×10^{14} to 1.09×10^{15} W/m^2. Subsequent frames show the conversions of k from 10 to 11, 12,...,15, indicating transitions to higher multiphoton processes.

The inset of Fig. 5 provides a magnified view of the calculation points near the experimental threshold intensity $I_{th}^{3.5} = 6 \times 10^{15}$ W/m^2 [16]. As for the near-infrared laser, we fit the low-intensity points to a linear curve, 3 for Keldysh (5.37×10^{15} to 6.48×10^{15} W/m^2), 4 for TDDFT (9.52×10^{14} to 9.52×10^{15} W/m^2), and 8 for SBE (1.00×10^{15} to 8.94×10^{15} W/m^2).

The slopes m obtained from the linear fitting, and the corresponding density of excited electrons n_{ex} at $I_{th}^{3.5}$, are tabulated in Table III.

For the 3 Keldysh points, their $k = 13$, $m = 6.42$, and γ ranging between 0.53 and 0.59. This means that in Keldysh model, the absorption mechanism includes some degree of tunneling. But not like TDDFT and SBE, where tunneling is dominating with the much lower slopes m.

The slopes m of the TDDFT and SBE curves are 1.26 and 1.97, respectively, suggesting that the transition mechanism is predominantly tunneling. In this scenario, under the influence of the strong laser field, the bands bend significantly, leading to a reduction in the potential barrier between the maximum of the valence band and the minimum of the conduction band. Electrons can then directly transition through this lowered barrier via the quantum tunneling effect, even without sufficient energy to overcome the band gap. The electronic excitations are determined by the interplay of the dominant intraband tunneling and the auxiliary interband MPA process. As the pump intensity continues to increase, even Keldysh shifts towards to tunneling domination ($\gamma \ll 1$), resulting in a reduced difference between the TDDFT results and the Keldysh model.

The value of $n_{ex}^{Keldysh}$ for 3.5-μm case is lower than the other two methods data, even within the constant electric field assumption, while $n_{ex}^{Keldysh}$ is larger than TDDFT and SBE in the MPA dominated 0.8-μm case. It also proves that the MPA percentage of Keldysh is more than others, and MPA alone cannot provide a sufficient number of excited electrons to achieve population inversion and lasing, which is consistent with Ref. [23].

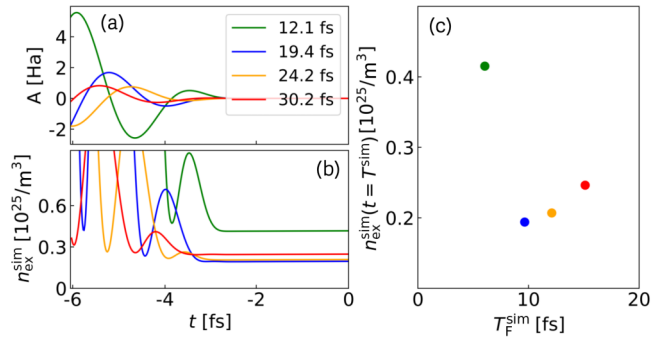


FIG. 6. The evolution of (a) the external vector potential $\boldsymbol{A}(t)$ and (b) the excited electrons density $n_{ex}^{sim}(t)$ for different propagation time T^{sim}. (c) Number of excited electrons $n_{ex}^{sim}(t = T^{sim})$ for the different simulation times.

D. Effect of different propagation time

In the experimental work of Ref. [57], the pulse durations are 30 fs (full width at half-maximum, FWHM) for 0.8 μm and 105 fs (FWHM) for 3.5 μm. Using the same propagation time as in the experiments is computationally prohibitive, therefore, we have adopted an alternative strategy to reduce the simulated time while still capturing the relevant physical effects.

We performed TDDFT simulations for different propagation time with full-propagation times T^{sim}: 12.1, 19.4, 24.2, and 30.2 fs. The FWHM time for these simulations T_F^{sim} is $T^{sim}/2$. The case with $T_F^{sim} = 15.1$ fs already consumes approximately 42 000 CPU hours and is only half of the $T_F^{expt} = 30$ fs used in the experiment of Ref. [57]. These simulations are done with the "unmodified" propagation scheme, with a wavelength of 0.8 μm and a peak intensity of 5×10^{15} W/m^2 before entering the ZnO crystal.

Figure 6(a) shows the tail of the vector potential employed, while the Fig. 6(b) displays the time evolution of the excited electron population $n_{ex}^{sim}(t)$ at the end-of-pulse region for different propagation time T^{sim}. The $n_{ex}^{sim}(t = T^{sim})$ values at the end of each pulse are listed in Table IV.

Since TDDFT does not include dissipation mechanisms, one expects that the longer the propagation time is, the more excited electrons remain in the conduction bands after the pulse ends. Counterintuitively, we observe that this is not the case going from the shortest propagation time $T^{sim} = 12.1$ fs to longer pulse durations. To better understand this, we compare the pump vector potential shape in Fig. 6(a). The 12.1-fs pulse contains only 2–3 optical cycles, resulting in a rather sharp envelope, which introduces a significant spectral broad-

TABLE IV. TDDFT calculated $n_{ex}(T^{sim})$ for different propagation times T^{sim} and FWHM times T_F^{sim}. The pump intensity is $I_{th}^{0.8} = 5 \times 10^{15}$ W/m^2.

T^{sim} (fs)	T_F^{sim} (fs)	$n_{ex}(T^{sim})$ (10^{25}/m^3)
12.1	6.1	0.4152
19.4	9.2	0.1941
24.2	12.1	0.2070
30.2	15.1	0.2463

ening of the laser pulse and carrier-envelope phase (CEP) effects. Thus, one cannot properly define the effective central frequency of such ultrashort pulse, and the tail of the pulse (between −6 to −3 fs) exhibits larger oscillations than other longer pulses, leading to the larger end value of $n_{\rm ex}^{\rm sim}(t)$.

In Fig. 4, all three methods adopt the same propagation time of 12.1 fs for the purpose of direct comparison between theoretical approaches. The resulting excitation density from TDDFT, $n_{\rm ex}^{\rm TDDFT} = 1.99 \times 10^{25}$ m^{-3}, as reported in Table II, happens to be very close to the reference data $n_{\rm ex}^{\rm Ref} = 2 \times 10^{25}$ m^{-3} [53]. This agreement is, however, a coincidence arising from accidental error cancellation.

In order to provide a meaningful comparison with the reference excitation density $n_{\rm ex}^{\rm Ref}$ at the experimental lasing threshold intensity $I_{\rm th}^{0.8}$, we plot the TDDFT data from Table IV in Fig. 6(c). This clearly highlights the transition between ultrashort pulses to longer ones, where CEP effects become negligible, and where the number of excited electrons becomes proportional to the pulse duration. Based on these results, we could extrapolate to estimate the excitation density at the FWHM time 30 fs, yielding $n_{\rm ex}^{\rm sim}(T_F^{\rm sim} = 30\ {\rm fs}) = 0.5 \times 10^{25}/{\rm m}^3$.

We note that during the excitation process, the transient excitation density $n_{\rm ex}^{\rm sim}(t)$ significantly exceeds $n_{\rm ex}^{\rm Ref} = 2 \times 10^{25}$ m^{-3} [53] for a long time. However, after the pump pulse ends, $n_{\rm ex}^{\rm sim}(t)$ stabilizes at a lower value $0.5 \times 10^{25}/{\rm m}^3$, which may seem to contradict the conditions required for laser emission.

This underestimation does not mean that the lasing process will not happen. Since TDDFT only describes electrons' excitation, not laser emission, it can only be used to know whether we arrive or not at the population inversion threshold, which is one of the necessary conditions of laser emission. In experiments, the emission of laser is usually an instantaneous behavior, and the population inversion states do not need to be maintained for a long time. As long as the conditions are met within the gain window and a certain period of time and there is cavity feedback, laser can be generated.

For the experimental case with $T_F^{\rm expt} = 105$ fs at 3.5 μm, a valid linear extrapolation would require simulations with $T_F^{\rm sim}$ approaching 50 fs, which exceeds our available computational resources. In Fig. 5, we instead use a propagation time of $T^{\rm sim} = 31.5$ fs, corresponding to $T_F^{\rm sim} = 15.8$ fs. Despite the shorter duration, this setup is sufficient to capture the underlying physical mechanism of electron excitation and clearly reveals the tunneling-dominated regime.

E. Dynamical Franz-Keldysh effect

The efficient sub-band-gap carrier excitation observed in our TDDFT simulations, particularly for mid-infrared pumping where the photon energy (0.354 eV) is an order of magnitude smaller than the ZnO band gap (3.3 eV), requires a microscopic understanding of the underlying physical mechanisms. To provide this insight, we analyze the optical response of ZnO under strong laser fields through the framework of the dynamical Franz-Keldysh effect (DFKE).

The DFKE analysis serves two key purposes in our study: (i) it provides a theoretical foundation for understanding how strong electric fields transiently modify the band structure and enable sub-band-gap transitions, and (ii) it offers an independent validation of the physical mechanisms captured by our TDDFT simulations. This analysis directly complements our comparison of multiphoton versus tunneling-dominated excitation regimes and helps explain why different theoretical approaches yield varying predictions for the same physical system.

Under irradiation by an intense laser field, the dielectric function $\epsilon(\omega)$ undergoes transient modification. The modification caused by a static electric field is known as the Franz-Keldysh effect (FKE) [58,59], while the modification caused by an alternating electric field is known as the DFKE [60,61].

The theoretical foundation for understanding Franz-Keldysh–type effects was significantly advanced by the pioneering work of Meier, Koch, and coworkers [24,62–64]. Their development of microscopic many-body theories, particularly for III-V semiconductor systems and superlattices, provided detailed insight into field-induced modifications of optical absorption under both static and dynamic field conditions. Their SBE framework for describing these effects represents a cornerstone in the field and is directly relevant to the DFKE phenomena we investigate.

The Keldysh parameter γ can also distinguish between these two regimes. The MPA applies for $\gamma \gg 1$, and the static FKE is appropriate for $\gamma \ll 1$, in the tunneling regime. For $\gamma \approx 1$, the DFKE phenomena are expected. We choose the experimental mid-IR pulse with $I_{\rm th}^{3.5} = 6 \times 10^{15}$ W/m^2, $\lambda = 3.5$ μm, and $\gamma = 0.55$ to explore DFKE in ZnO, as the other experimental near-IR laser has a larger $\gamma = 2.61$ which exceeds our required range.

We apply a full-frequency δ function $E_0\delta(t - t_0)\hat{e}_z$ to "kick" the electrons in our simulation cell and probe the optical information after electrons are excited to conduction bands by the experimental mid-infrared pump pulse. Here, $t_0 = 29$ fs is the time delay between the probe and pump pulse, and the total propagation time is 36.3 fs. The "kick" strength is $A_0 = 2.7$ eV after gauge transforming via Eq. (16), and $\hat{e}_z$ is the polarization direction of the "kick."

The induced-electric field evolution due to the pump pulse and "kick" probe are illustrated in Fig. 7(a). The amplitude of the pump pulse is 1000 times larger than the one of the probe, hence, near 29 fs, the "kick" is observed as a minuscule bump, that is magnified for clarity in the inset of Fig. 7.

Next, we carried out a pure pump propagation and calculated the difference of the induced vector potential $\boldsymbol{A}_{\rm ind}$ between "pump + probe" and "pump only" simulations to extract the response to the "kick" after the electrons are excited to the conduction bands by the pump pulse. This result is shown in Fig. 7(b). For consistency, we convert the vector potential $\boldsymbol{A}$ to the electric field $\boldsymbol{E}$ via Eq. (16).

From the information of induced field $\boldsymbol{A}_{\rm ind}(t)$, we can calculate the dielectric function $\epsilon(\omega)$ as given by Eq. (25). Here, the parameters t_0 and A_0 represent the delay time and strength of the probe pulse, respectively. ω is the laser frequency

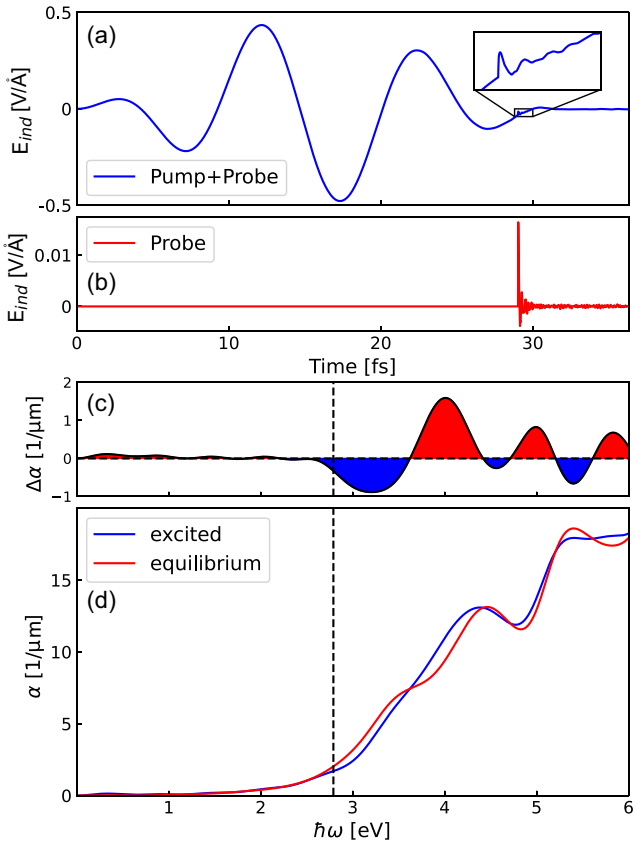


FIG. 7. (a) The induced electric field $\boldsymbol{E}_{\text{ind}}$ of the mid-IR *pump* pulse and weak "kick" *probe* with 29-fs delay. (b) The extracted "kick" *probe* response is equal to (*pump* + *probe*)-*pump*. (c) The difference of absorption coefficients $\Delta\alpha(\omega)$ calculated from (d) the absorption coefficient in the excited and equilibrium states. The black dashed line represents the calculated DFT + U band-gap value 2.81 eV.

for 3.5-μm case, and the time step $dt = 3.6 \times 10^{-4}$ fs. The denominator is the degenerate form of $\int_{0_+}^{T} e^{i\omega t} \frac{d\boldsymbol{A}_{\text{ext}}(t)}{dt} dt$ with $\boldsymbol{E}_{\text{ext}} = -1/c \cdot d\boldsymbol{A}_{\text{ext}}(t)/dt = E_0 \delta(t - t_0)\hat{e}_z$:

$$\frac{1}{\epsilon(\omega)} = 1 + \frac{\int_{0_+}^{T} e^{i\omega t} \cdot D(t) \cdot \frac{d\boldsymbol{A}_{\text{ind}}(t)}{dt} dt}{e^{i\omega t_0} A_0}. \tag{25}$$

The damping function $D(t)$ is used to reduce the tail fluctuation during Fourier transform, and $\eta = 0.3$ eV is the damping strength:

$$D(t) = \begin{cases} \exp[-\eta(t - t_0)], & \text{if } t_0 < t < T \\ 1, & \text{if } 0 < t \leqslant t_0. \end{cases} \tag{26}$$

Subsequently, we can calculate the absorption coefficient $\alpha(\omega)$ using Eq. (27) with unit of 1/μm:

$$\alpha(\omega) = \frac{4\pi}{\lambda} \sqrt{\frac{|\epsilon| - \epsilon_1}{2}}. \tag{27}$$

Here, $|\epsilon|$ and ϵ_1 denote the absolute value and the real part of the dielectric function, respectively. The absorption coefficient $\alpha(\omega)$ is utilized in the Beer-Lambert absorption law $I_{\text{out}} = I_{\text{in}} e^{-\alpha(\omega)d}$, where I_{in} and I_{out} represent the input and output intensity, respectively, and d in μm is the absorption length.

In Fig. 7(d), we compare the absorption spectrum $\alpha(\omega)$ of excited states (blue solid line), which reveals the optical properties after electrons are excited to the conduction bands by pump pulse, and $\alpha(\omega)$ of equilibrium states (red solid line), where the electrons are still in the valence bands without pump.

Their difference is shown in Fig. 7(c), $\Delta\alpha(\omega) = \alpha_{\text{excited}}(\omega) - \alpha_{\text{equilibrium}}(\omega)$, illustrating the absorption changes attributed to the DFKE: slight absorption occurs below the calculated DFT + U band edge 2.81 eV; near the band edge ($\hbar\omega \sim E_g$), the first negative blue zone, shows $\alpha_{\text{excited}} < \alpha_{\text{equilibrium}}$, indicating a blueshift of the band edge; and oscillatory behavior is observed above the band edge. All the characteristic features of the DFKE are reproduced for the 3.5-μm pump at the experimental threshold intensity $I_{\text{th}}^{3.5}$.

IV. CONCLUSIONS

We employed three complementary theoretical approaches to study the excitation mechanism in ZnO bulk: the analytical Keldysh model, the four-bands model of the semiconductor Bloch equations (SBE), and real-time time-dependent density functional theory (TDDFT) simulations, for two different pump laser wavelengths.

For the near-IR 0.8-μm pump laser, all three theoretical methods indicate that interband multiphoton absorption is the dominant excitation mechanism near the experimental laser threshold intensity [16] $I_{\text{th}}^{0.8} = 5 \times 10^{15}$ W/m^2. Additionally, SBE and TDDFT reveal that intraband tunneling plays a contributing role.

In the mid-IR 3.5-μm pump case, at the experimental laser threshold intensity [16] $I_{\text{th}}^{3.5} = 6 \times 10^{15}$ W/m^2, all three methods show that the excitation mechanism is determined by the interplay of dominating intraband tunneling and auxiliary interband multiphoton absorption.

We have also successfully reproduced the dynamical Franz-Keldysh effect for the mid-IR pump case with TDDFT, and observed its main characteristic features. In summary, TDDFT calculations offer an accurate description of the transformation of excitation mechanisms for different pump wavelengths and different pump intensities under ultrashort laser pulse irradiation in ZnO. Further quantitative predictions and simulations based on TDDFT are expected to boost the search for novel materials and phenomena.

ACKNOWLEDGMENT

This research is supported by the German Research Foundation (DFG) under Project No. CRC/SFB 1375 "NOA–Nonlinear Optics down to Atomic scales".

DATA AVAILABILITY

The data that support the findings of this study are available from the corresponding author upon reasonable request.

[1] J. Kim, S. K. Lee, J.-H. Lee, H.-Y. Kim, N. H. Kim, C. H. Lee, C.-S. Lee, and H. G. Kim, ZnO nanowire-based early detection of SARS-CoV-2 antibody responses in asymptomatic patients with COVID-19, Adv. Mater. Interfaces **9**, 2102046 (2022).

[2] S. Baruah, M. Jaisai, R. Imani, M. M. Nazhad, and J. Dutta, Photocatalytic paper using zinc oxide nanorods, Sci. Technol. Adv. Mater. **11**, 055002 (2010).

[3] S. Tian, F. Yang, D. Zeng, and C. Xie, Solution-processed gas sensors based on ZnO nanorods array with an exposed (0001) facet for enhanced gas-sensing properties, J. Phys. Chem. C **116**, 10586 (2012).

[4] X. Li, X. Liu, Y. Li, D. Gao, and L. Cao, Using novel semiconductor features to construct advanced ZnO nanowires-based ultraviolet photodetectors: A brief review, IEEE Access **9**, 11954 (2021).

[5] F. H. Nicoll, Ultraviolet ZnO laser pumped by an electron beam, Appl. Phys. Lett. **9**, 13 (1966).

[6] D. M. Bagnall, Y. F. Chen, Z. Zhu, T. Yao, S. Koyama, M. Y. Shen, and T. Goto, Optically pumped lasing of ZnO at room temperature, Appl. Phys. Lett. **70**, 2230 (1997).

[7] P. Yu, Z. K. Tang, G. K. L. Wong, M. Kawasaki, A. Ohtomo, H. Koinuma, and Y. Segawa, Room-temperature gain spectra and lasing in microcrystalline ZnO thin films, J. Cryst. Growth. **184–185**, 601 (1998).

[8] T. Makino, Y. Segawa, M. Kawasaki, and H. Koinuma, Optical properties of excitons in ZnO-based quantum well heterostructures, Semicond. Sci. Technol. **20**, S78 (2005).

[9] M. Huang, S. Mao, H. Feick, H. Yan, Y. Wu, H. Kind, E. Weber, R. Russo, and P. Yang, Room-temperature ultraviolet nanowire nanolasers, Science **292**, 1897 (2001).

[10] L. Mädler, W. J. Stark, and S. E. Pratsinis, Rapid synthesis of stable ZnO quantum dots, J. Appl. Phys. **92**, 6537 (2002).

[11] Ü. Özgür, Y. I. Alivov, C. Liu, A. Teke, M. A. Reshchikov, S. Dogan, V. Avrutin, S.-J. Cho, and H. Morkoc, A comprehensive review of ZnO materials and devices, J. Appl. Phys. **98**, 041301 (2005).

[12] R.-M. Ma and R. F. Oulton, Applications of nanolasers, Nat. Nanotech. **14**, 12 (2019).

[13] D. H. Jones and H. R. Reiss, Intense-field effects in solids, Phys. Rev. B **16**, 2466 (1977).

[14] S. J. Hua and W. D. Zhang, Multiphoton absorption and dispersive nonlinear refraction of ZnO in VIS-NIR bands, Opt. Laser. Technol. **145**, 107478 (2022).

[15] S. K. Das, M. Biswas, D. Byrne, M. Bock, E. McGlynn, M. Breusing, and R. Grunwald, Multiphoton-absorption induced ultraviolet luminescence of ZnO nanorods using low-energy femtosecond pulses, J. Appl. Phys. **108**, 043107 (2010).

[16] R. Hollinger, P. Malevich, V. Shumakova, S. Alisauskas, M. Zapf, R. Röder, A. Pugžlys, A. Baltuška, C. Ronning, C. Spielmann, and D. Kartashov, Strong light-field driven nanolasers, Nano Lett. **19**, 3563 (2019).

[17] S. Ghimire, A. D. DiChiara, E. Sistrunk, U. B. Szafruga, P. Agostini, L. F. DiMauro, and D. A. Reis, Redshift in the optical absorption of ZnO single crystals in the presence of an intense midinfrared laser field, Phys. Rev. Lett. **107**, 167407 (2011).

[18] R. Boge, C. Cirelli, A. S. Landsman, S. Heuser, A. Ludwig, J. Maurer, M. Weger, L. Gallmann, and U. Keller, Probing nonadiabatic effects in strong-field tunnel ionization, Phys. Rev. Lett. **111**, 103003 (2013).

[19] See Supplemental Material at http://link.aps.org/supplemental/10.1103/p3r8-6grq for further details on the calculation of dipole matrix elements; the impact of dephasing time on the SBE solution; the influence of band-gap errors on the SBE and Keldysh model; and the intensity-dependent optical parameters in TDDFT.

[20] L. V. Keldysh, Ionization in the field of a strong electromagnetic wave, Zh. Eksp. Teor. Fiz. **47**, 1945 (1964).

[21] S. V. Popruzhenko, Keldysh theory of strong field ionization: History, applications, difficulties and perspectives, J. Phys. B: At., Mol. Opt. Phys. **47**, 204001 (2014).

[22] L. A. Siiman, J. Lumeau, and L. B. Glebov, Nonlinear photoionization and laser-induced damage in silicate glasses by infrared ultrashort laser pulses, Appl. Phys. B **96**, 127 (2009).

[23] T. J.-Y. Derrien, N. Tancogne-Dejean, V. P. Zhukov, H. Appel, A. Rubio, and N. M. Bulgakova, Photoionization and transient Wannier-Stark ladder in silicon: First-principles simulations versus Keldysh theory, Phys. Rev. B **104**, L241201 (2021).

[24] M. Lindberg and S. W. Koch, Effective Bloch equations for semiconductors, Phys. Rev. B **38**, 3342 (1988).

[25] Y. Lun and B. G. Mette, Introduction to theory of high-harmonic generation in solids: Tutorial, J. Opt. Soc. Am. B **39**, 535 (2022).

[26] I. Floss, C. Lemell, G. Wachter, V. Smejkal, S. A. Sato, X.-M. Tong, K. Yabana, and J. Burgdörfer, *Ab initio* multiscale simulation of high-order harmonic generation in solids, Phys. Rev. A **97**, 011401(R) (2018).

[27] G. Vampa, C. R. McDonald, G. Orlando, D. D. Klug, P. B. Corkum, and T. Brabec, Theoretical analysis of high-harmonic generation in solids, Phys. Rev. Lett. **113**, 073901 (2014).

[28] T. T. Luu, M. Garg, S. Y. Kruchinin, A. Moulet, M. T. Hassan, and E. Goulielmakis, Extreme ultraviolet high-harmonic spectroscopy of solids, Nature (London) **521**, 498 (2015).

[29] T. T. Luu and H. J. Wörner, High-order harmonic generation in solids: A unifying approach, Phys. Rev. B **94**, 115164 (2016).

[30] M. Kira and S. W. Koch, Many-body correlations and excitonic effects in semiconductor spectroscopy, Prog. Quantum Electron. **30**, 155 (2006).

[31] H. Akima, A new method of interpolation and smooth curve fitting based on local procedures, J. ACM **17**, 589 (1970).

[32] J. Peinado, J. Ibáñez, E. Arias, and V. Hernández, Adams–Bashforth and Adams–Moulton methods for solving differential Riccati equations, Comput. Math. Appl. **60**, 3032 (2010).

[33] E. Runge and E. K. U. Gross, Density-functional theory for time-dependent systems, Phys. Rev. Lett. **52**, 997 (1984).

[34] T. Otobe, M. Yamagiwa, J.-I. Iwata, K. Yabana, T. Nakatsukasa, and G. F. Bertsch, First-principles electron dynamics simulation for optical breakdown of dielectrics under an intense laser field, Phys. Rev. B **77**, 165104 (2008).

[35] K. Yabana, T. Sugiyama, Y. Shinohara, T. Otobe, and G. F. Bertsch, Time-dependent density functional theory for strong electromagnetic fields in crystalline solids, Phys. Rev. B **85**, 045134 (2012).

[36] N. Tancogne-Dejean, M. A. Sentef, and A. Rubio, Ultrafast transient absorption spectroscopy of the charge-transfer insulator NiO: Beyond the dynamical Franz-Keldysh effect, Phys. Rev. B **102**, 115106 (2020).

[37] K. Yabana, T. Nakatsukasa, J.-I. Iwata, and G. F. Bertsch, Real-time, real-space implementation of the linear response

time-dependent density-functional theory, Phys. Status Solidi B **243**, 1121 (2006).
[38] G. Le Breton, A. Rubio, and N. Tancogne-Dejean, High-harmonic generation from few-layer hexagonal boron nitride: Evolution from monolayer to bulk response, Phys. Rev. B **98**, 165308 (2018).
[39] D. R. Hamann, Optimized norm-conserving Vanderbilt pseudopotentials, Phys. Rev. B **88**, 085117 (2013).
[40] J. P. Perdew, K. Burke, and M. Ernzerhof, Generalized gradient approximation made simple, Phys. Rev. Lett. **77**, 3865 (1996).
[41] N. Tancogne-Dejean, M. J. T. Oliveira, and A. Rubio, Self-consistent DFT + U method for real-space time-dependent density functional theory calculations, Phys. Rev. B **96**, 245133 (2017).
[42] L. A. Agapito, S. Curtarolo, and M. Buongiorno Nardelli, Reformulation of DFT + U as a pseudohybrid Hubbard density functional for accelerated materials discovery, Phys. Rev. X **5**, 011006 (2015).
[43] M. Schultze, K. Ramasesha, C. Pemmaraju, S. Sato, D. Whitmore, A. Gandman, J. S. Prell, L. J. Borja, D. Prendergast, K. Yabana, D. M. Neumark, and S. R. Leone, Attosecond band-gap dynamics in silicon, Science **346**, 1348 (2014).
[44] C. Ullrich, *Time-Dependent Density-Functional Theory: Concepts and Applications* (Oxford University Press, Oxford, 2012).
[45] A. Castro, H. Appel, M. Oliveira, C. A. Rozzi, X. Andrade, F. Lorenzen, M. A. L. Marques, E. K. U. Gross, and A. Rubio, Octopus: A tool for the application of time-dependent density functional theory, Phys. Status Solidi B **243**, 2465 (2006).
[46] N. Tancogne-Dejean, M. J. T. Oliveira, X. Andrade, H. Appel, C. H. Borca, G. Le Breton, F. Buchholz, A. Castro, S. Corni, A. A. Correa, U. De Giovannini, A. Delgado, F. G. Eich, J. Flick, G. Gil, A. Gomez, N. Helbig, H. Hübener, R. Jestädt, J. Jornet-Somoza, *et al.*, Octopus, a computational framework for exploring light-driven phenomena and quantum dynamics in extended and finite systems, J. Chem. Phys. **152**, 124119 (2020).
[47] H. Karzel, W. Potzel, M. Köfferlein, W. Schiessl, M. Steiner, U. Hiller, G. M. Kalvius, D. W. Mitchell, T. P. Das, P. Blaha, K. Schwarz, and M. P. Pasternak, Lattice dynamics and hyperfine interactions in ZnO and ZnSe at high external pressures, Phys. Rev. B **53**, 11425 (1996).
[48] H. J. Monkhorst and J. D. Pack, Special points for Brillouin-zone integrations, Phys. Rev. B **13**, 5188 (1976).
[49] A. Gómez Pueyo, M. A. L. Marques, A. Rubio, and A. Castro, Propagators for the time-dependent Kohn–Sham equations: Multistep, Runge–Kutta, exponential Runge–Kutta, and commutator free Magnus methods, J. Chem. Theory Comput. **14**, 3040 (2018).
[50] G. F. Bertsch, J. Giansiracusa, and K. Yabana, Application of time-dependent density-functional theory to electron—ion coupling in ethylene, Isr. J. Chem. **42**, 151 (2002).
[51] V. Turkowski and C. A. Ullrich, Time-dependent density-functional theory for ultrafast interband excitations, Phys. Rev. B **77**, 075204 (2008).
[52] V. Turkowski, A. Leonardo, and C. A. Ullrich, Time-dependent density-functional approach for exciton binding energies, Phys. Rev. B **79**, 233201 (2009).
[53] M. A. M. Versteegh, T. Kuis, H. T. C. Stoof, and J. I. Dijkhuis, Ultrafast screening and carrier dynamics in ZnO: Theory and experiment, Phys. Rev. B **84**, 035207 (2011).
[54] M. Wu, S. Ghimire, D. A. Reis, K. J. Schafer, and M. B. Gaarde, High-harmonic generation from Bloch electrons in solids, Phys. Rev. A **91**, 043839 (2015).
[55] J. D. Jackson, *Classical Electrodynamics* (Wiley, Hoboken, NJ, 2021).
[56] A. Yamada and K. Yabana, Energy transfer from intense laser pulse to dielectrics in time-dependent density functional theory, Eur. Phys. J. D **73**, 87 (2019).
[57] R. Hollinger, D. Gupta, M. Zapf, M. Karst, R. Röder, I. Uschmann, U. Reislöhner, D. Kartashov, C. Ronning, and C. Spielmann, Polarization dependent multiphoton absorption in ZnO thin films, J. Phys. D: Appl. Phys. **53**, 055102 (2020).
[58] W. Franz, Einfluß eines elektrischen feldes auf eine optische absorptionskante, Z. Naturforsch. A **13**, 484 (1958).
[59] L. Keldysh, in *Selected Papers of Leonid V Keldysh* (World Scientific, Singapore, 2024).
[60] A. P. Jauho and K. Johnsen, Dynamical Franz-Keldysh effect, Phys. Rev. Lett. **76**, 4576 (1996).
[61] K. B. Nordstrom, K. Johnsen, S. J. Allen, A.-P. Jauho, B. Birnir, J. Kono, T. Noda, H. Akiyama, and H. Sakaki, Excitonic dynamical Franz-Keldysh effect, Phys. Rev. Lett. **81**, 457 (1998).
[62] T. Meier, H. Kolbe, A. Thränhardt, G. Weiser, P. Thomas, and S. Koch, Coherent dynamics of photoexcited semiconductor superlattices in homogeneous electric fields, Phys. E (Amsterdam) **7**, 267 (2000).
[63] T. Meier, G. von Plessen, P. Thomas, and S. W. Koch, Coherent effects induced by static and time-dependent electric fields in semiconductors, Phys. Rev. B **51**, 14490 (1995).
[64] H. Haug and S. Koch, *Quantum Theory of the Optical and Electronic Properties of Semiconductors*, G - Reference,Information and Interdisciplinary Subjects Series (World Scientific, Singapore, 2009).